Monitoring ion beam therapy with a Compton Camera: simulation studies of the clinical feasibility

M. Fontana[1] **and J.-L. Ley**[1]**, S.Brons**[4]**, D. Dauvergne**[3]**,**
N. Freud[2]**, J. Krimmer**[1]**, J. M. Létang**[2]**, V. Maxim**[2]**,**
M.-H. Richard[1]**, I. Rinaldi**[5]**, and É. Testa**[1]

[1]Univ Lyon, Université Claude Bernard Lyon 1, CNRS/IN2P3, Institut de Physique Nucléaire de Lyon, 69622 Villeurbanne, France
[2]Univ Lyon, INSA-Lyon, Université Claude Bernard Lyon 1, UJM-Saint Étienne, CNRS, Inserm, Centre Léon Bérard, CREATIS UMR 5220 U1206, F-69373, Lyon, France
[3]Université Grenoble Alpes, CNRS, Grenoble INP, LPSC-IN2P3, 38000 Grenoble, France
[4]Heidelberg ion therapy center - Heidelberger Ionenstrahl-Therapiezentrum (HIT), Im Neuenheimer Feld 450, 69120 Heidelberg
[5]Department of Radiation Therapy and Oncology, Heidelberg University Hospital, Im Neuenheimer Feld 400, 69120 Heidelberg, Germany, now at MAASTRO Clinic, Dr. Tanslaan 12, 6229 ET Maastricht, The Netherlands

E-mail: `m.fontana@ipnl.in2p3.fr`

Abstract.
As more and more particle therapy centers are being built world-wide, there is increasing need in treatment monitoring methods, ideally in real-time. The present work investigates the clinical applicability of a Compton camera design by means of Monte Carlo simulations. The Compton camera performance has been studied with the simulation of point-like source and beam irradiation of a PMMA phantom. The system absolute photon detection efficiency, measured via source irradiation, varies in the range $[1,4] \times 10^{-4}$ with energy variations in the prompt gamma energy range and source position shifts with respect to the center of the camera. With proton and carbon beams impinging on a PMMA cylindrical phantom, the number of detected prompt-gamma coincidences related to various beam time structure has been studied. Finally, the accuracy of the camera in identifying the dose profile fall-off position has been estimated and two different event reconstruction methods have been compared for this purpose; one based on analytical calculation with a line-cone technique, the second relying on an iterative MLEM algorithm. Both methods showed the possibility to reconstruct the beam depth-dose profile and to retrieve the dose fall-off with millimeter precision on a spot basis.

Contents

1. Introduction

Ion beam therapy is a cancer treatment technique which is rapidly gaining importance in the global tumor therapy panorama. In addition to the seventy already operational clinical facilities, with more than 175000 patients already treated by the end of 2017, several new centers have been designed and approved for construction worldwide [Particle Therapy Cooperative Group, 2017]. The favorable feature of this treatment technique is connected to the peculiar energy deposition profile of charged particles as a function of depth in matter. As first observed by Bragg [Bragg and Kleeman, 1904], the depth-dose profile of charged particles shows a maximum close to the end of their range in matter; in addition to this, a strong enhancement of the relative biological effectiveness (RBE) is observed for ions heavier than protons in the region of the Bragg peak [Elsässer et al., 2004, Weyrather et al., 1999], which further enhances the dose ratio between target and healthy tissues.

The maximum of the dose is deposited in the Bragg peak region in the patient and must be tuned to cover the target volume (defined via CT scan) and, at the same time, spare the surrounding healthy tissues. Treatment planning and delivery uncertainties, like uncertainties in the material composition determination, CT units conversion to ion stopping power, patient mis-positioning, organ motion or morphological changes between treatment fractions, limit the tumour targeting capabilities. These uncertainties force the clinicians to fix relatively large safety margins around the planned treatment volume, up to $3.5\% + 3$ mm [Paganetti, 2012]. Ion-range verification is one of the conditions required for a broader usage of ion beam therapy and for its further development. With the goal of fully exploiting the ion beam therapy dosimetric potential, the monitoring should be in real-time and ideally in 3 dimensions, in order to detect important deviations between the planned and delivered dose to the target volume or to surrounding organs, in particular in case of proximity to organs-at-risk (OAR). This capability would allow for a reduction of the above mentioned safety margins and for a better tumor targeting; in addition to this, it could permit the use of new irradiation fields with OAR downstream with respect to the tumor position [Knopf and Lomax, 2013].

Several range verification techniques have been considered worldwide for twenty years. Most of them rely on the detection of secondary radiation generated during the slowing down process of incident ions, in particular during nuclear reactions. Among theses secondary radiations, positron emitters have been deeply studied in order to exploit positron emission tomography (PET) machines for treatment monitoring. The only available and functional range monitoring systems in a clinical center are based on this technique [Enghardt et al., 2004, Yamaya, 2018], which is anyway affected by physical and technical limitations [Parodi, 2016].

In addition to positron annihilation products, the relaxation of excited nuclei also produces secondary photons in a wide energy range, between some

hundreds of keV till about 8-10 MeV. After the first proposal published in 2003 [Stichelbaut and Jongen, 2003], these secondary products of particle treatment have been deeply investigated and the correlation of this gamma radiation to the ion depth-dose profile has been confirmed by several research groups, starting from [Min et al., 2006] for protons and [Testa et al., 2008] for carbon ions. The so-called prompt gamma-rays (PG) have the advantage to be emitted almost instantaneously after the beam interaction in the tissue, making them more adapted than PET 511 keV gammas for real-time monitoring. Moreover, as shown in [Robert et al., 2013], the emission rate is comparable to or larger than the one of the annihilation gammas for both protons and carbon beams. Consequently, different techniques have been proposed to exploit this signal for treatment monitoring purpose, with the related detection systems. For a review on PG monitoring, see [Krimmer et al., 2017].

Originally designed for astrophysics applications, the potential of Compton cameras for medical imaging has been soon recognized [Todd et al., 1974] and then directly translated to the ion beam therapy monitoring domain. Such a gamma detection system is generally composed of two sections: a scatterer and an absorber. The scatterer is dedicated to the gamma Compton-scattering, and should be designed to optimize the Compton scattering probability in the prompt gamma energy range, while reducing the so-called Doppler broadening effect due to electron binding and motion [Ordonez et al., 1997]; in most of the cases, this leads to the choice of a light material (low Z), segmented in several subsections. On the other hand, heavier materials may be used to improve photon detection efficiency ([Solevi et al., 2016, Aldawood et al., 2017, Polf et al., 2015]). The absorber finally intends to capture the Compton scattered photons via photoelectric effect and is often composed of segmented high-Z scintillating materials. A slightly different Compton camera configuration can also achieve Compton electron tracking in the scattering detector [Frandes et al., 2010, Yoshihara et al., 2017], which results in additional information for the further reconstruction algorithm. The collected interaction positions and energy depositions in the two detector sections are used to constrain the emission point to the surface of a cone (or to a segment in the cone if the Compton electron track information is retrieved), via Compton kinematics (for an electron initially at rest):

$$\cos\theta = 1 - \frac{m_e c^2 E_1}{E_2(E_1 + E_2)}, \tag{1}$$

where $m_e c^2 = 511$ keV, E_1 and E_2 are the energies, respectively, deposited in the scatterer and the absorber. Analytic or iterative algorithms use these cones to create the image of the prompt gamma emission distribution, with intrinsic 3 dimensional capability [Wilderman et al., 1998, McKisson et al., 1994, Kuchment and Terzioglu, 2016, Maxim, 2018].

Several sources of uncertainty and signal background are connected to the above described detection method. The reported Compton kinematics formula (equation 1)

assumes valid the relation:

$$E_0 = E_1 + E_2. \tag{2}$$

Since the initial photon energy (E_0) is not known a priori, a complete photon energy absorption is needed for the cone calculation, or at least three Compton scattering interactions in the camera are required in a single event. An under-estimation of the total initial energy (caused by a photon non-complete absorption in the absorber section or by the Compton electron escape from the scatterer section), leads to a mis-estimation of the Compton angle, so to a Compton cone reconstruction uncertainty. If triple scattered photons are selected, the initial photon energy can be calculated analytically so that a complete absorption is not mandatory. In addition to this, the Compton formula considers the Compton scattering electron initially at rest, and its energy configuration creates a blur in the Compton angle reconstruction, resulting in the already cited Doppler broadening effect [Ordonez et al., 1997]. Furthermore, the detection principle is based on time coincidences between the two detector sections, therefore the time structure of the incoming particles plays an important role. The final image accuracy suffers from random coincidences generated by two prompt gammas interacting within the same time window or by contamination of secondaries, mainly neutrons and protons. The effect of random coincidences can be reduced by high detector time resolution or background rejection methods [Draeger et al., 2017]. Energy selections can be applied to the collected coincidences [Polf et al., 2009, Hilaire et al., 2016] and the homogeneous neutron background can be reduced via time-of-flight information [Testa et al., 2010].

Ortega et al. [Ortega et al., 2015] presented a detailed analysis of the noise sources for Compton imaging in proton therapy monitoring, and the clinical application of this method for detecting range shifts was tested for the setup under development in Valencia. The simulation study showed the relative expected rate of prompt gammas and neutrons, and the resulting rate of random coincidences ranging from 19 % to more than 60 % depending on the beam energy and the coincidence time window. This amount of fake events leads to complex reconstruction scenarios, where the identification of a 3 mm range shift is not clear for all cases.

Starting from these results, we propose in this paper to study with Monte Carlo simulations a Compton camera prototype based on semiconductor and scintillator detectors [Krimmer et al., 2015, Fontana et al., 2018] developed by the CLaRyS collaboration, involving four French research institutions.

The camera performance is studied with respect to the gamma energy in the prompt gamma energy range. Furthermore, the feasibility of its clinical application as depth-dose profile monitor during ion beam therapy clinical treatment is analyzed. After a preliminary study with point-like gamma sources irradiation focused on detector efficiency measurements as a function of the source position and gamma energy, clinical proton and carbon beams impinging on an homogeneous PMMA phantom are simulated to reproduce treatment conditions and analyze the prompt gamma detection resulting scenario. The ratio between true and random coincidences is studied as a function of
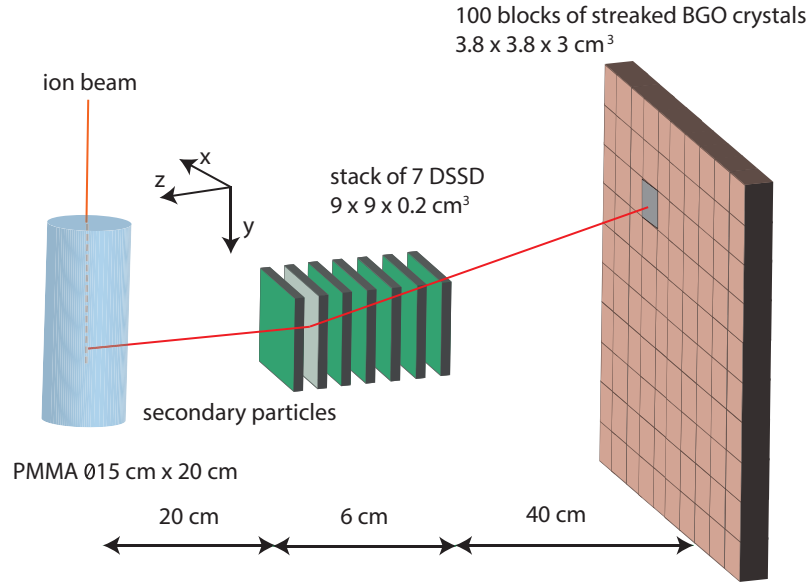
Figure 1: Scheme of the simulation setup (not at scale): a PMMA cylindrical phantom is set in front of the Compton camera prototype. The Compton camera is composed of a stack of 7 double sided silicon strip detectors (scatterer) and a plane of 100 single BGO blocks. The set distances are realistic for clinical conditions. This geometrical configuration has been used for all the simulations presented in this work.

the beam intensity. Two kinds of reconstruction algorithms, a line-cone analytic method and a MLEM iterative one, are applied to the collected data in order to compare the imaging results. Finally, the precision with which the dose profile fall-off can be detected with the Compton camera is reported.

2. Material and methods

2.1. Simulation setup

The monitoring system modeled in this simulation work is the Compton camera prototype under development within the French collaboration CLaRyS. The detectors detailed characteristics can be found in [Krimmer et al., 2015].

The scatterer consists of seven parallel planes of silicon detectors (double-sided silicon strip detectors, DSSDs), $9 \times 9 \times 0.2$ cm^3, with 1 cm distance between the centers of two neighboring planes, while the absorber is composed of an array of 10×10 BGO (Bismuth Germanate - $Bi_{12}GeO_{20}$) blocks ($3.5 \times 3.5 \times 3.0$ cm^3 each) placed behind the silicon layers at a distance which can be tuned according to the requirements.

The silicon detectors have a strip pitch of 1.4 mm, for a total of 64 strips per side (double-sided readout based on electron and hole pairs collection). Regarding the BGO blocks, their entrance surface is streaked in a 8×8 matrix of pseudo-pixels,

4.4×4.4 mm^2 size, and the readout is performed via 4 photo-multiplier tubes. The position reconstruction is achieved via Anger logic [Fontana et al., 2018].

A scheme of the simulation setup is given in Figure 1. The ion beam interacts with a cylindrical PMMA (PolyMethylMethAcrylate) phantom (15 cm diameter and 20 cm length) placed in front of the Compton camera as target. It is placed 20 cm far from the first silicon plane (center-to-center distance) which seems a realistic distance in clinical conditions. The distance between the last silicon layer and the absorber array (center-to-center) is set to 40 cm in order to enable time-of-flight measurements (see section 2.4).

The silicon detector strips are not reproduced in the simulation code, and the spatial resolution in the detector plane is set to 0.9 mm FWHM at the reference energy of 1 MeV, according to preliminary measurements performed on smaller detector prototypes. In the plane of the detectors (xy in Figure 1), interactions are defined as localized energy deposits, and the events presenting multiple hits separated by a distance beyond 3-strip equivalent are rejected. For the accepted multiple-hit interactions, the interaction position in the detector plane is defined as the center of gravity of the hits, weighted with the hit energy deposit. Concerning the direction perpendicular to the detector plane (z axis in Figure 1), the interaction position is set to the center of the involved silicon plane. A mono-block crystal is simulated for the absorber for simplicity. The events are selected to be limited to a single block component based on the interaction localization, and, as for the scatterer layers, the interaction position is reconstructed via center of gravity calculation if multiple interactions occur within the same block. An uncertainty contribution, randomly extracted by a Gaussian of 5 mm FWHM (corresponding to an overestimation of the geometrical resolution given by the pseudo-pixel matrix, set to reproduce not yet tested experimental conditions), is added to the reconstructed position to mimic the pseudo-pixel-based readout. For what concerns the z direction, given the fact that the employed BGO blocks have not depth of interaction reconstruction capabilities, the interaction position is fixed to the center of the mono-block crystal.

The energy resolution of the silicon detector is set to 5 keV (FWHM) for an energy deposit of 200 keV according to the design expectations, and varies as a function of $\sqrt{E_1}$. The energy resolution of the BGO blocks was estimated in preliminary measurements and is accordingly set to 20% FWHM at the reference energy of 667 keV (a 137-cesium source has been used for the measurements).

The time resolution has been set to 15.0 ns FWHM for the silicon slabs and to 3.0 ns FWHM for the BGO blocks, according to preliminary measurements performed on test detector modules at the GANIL center in France.

The detector resolutions play an important role in the Compton camera performances. The spatial resolution of the absorber influences the axis orientation of the Compton cone. The energy resolutions of the two detector sections determine the Compton cone aperture angle. The time resolution impacts the coincidence window between the absorber and the scatterer, and therefore the detectors ability to distinguish between true and random coincidences.

Table 1: Estimations of reachable resolutions with the detectors. Those resolutions are applied during the simulations.

Resolution (FWHM) at 1 MeV	Scatterer	Absorber	Hodoscope
spatial [mm]	0.9	5	1
energy	11 keV	20 %	/
timing [ns]	15	3	1

Table 2: Hadronic models used in the Geant4 simulations.

Process	Protons	Ions	Neutrons
Electromagnetic		standard$_{option3}$	
Inelastic	G4BinaryCascade	G4QMDReaction	G4BinaryCascade
		(G4IonsShenCrossSection)	+ G4NeutronHPInelastic (<19 MeV)
Elastic	G4LElastic	G4LElastic	G4LElastic + G4NeutronHPElastic (<19 MeV)
Fission	/	/	G4LFission + G4NeutronHPFission(<19 MeV)
Capture	/	/	G4LCapture + G4NeutronHPCapture (<19 MeV)
Radioactivedecay	/	G4Radioactivedecay	/

The CLaRyS project also includes the development of a beam tagging hodoscope, composed of scintillating fibers read out by multi-channel photomultipliers. This detector is used to synchronize the beam time and space structure to the prompt gamma detection in order to tune the detection window reducing the background contamination. In addition to this, the spatial localization of the impinging beam bunch can be included in the event reconstruction algorithm to add constraints to the obtained solutions (see section 2.5). The hodoscope is not included in the simulation, but its spatial and time resolution have to be taken into account for the time-of-flight discrimination (see section 2.4) and events reconstruction. They are set to 1 ns and 1 mm FWHM, respectively. The detector's spatial, energy, and time resolutions are summarized in table 1.

The Monte Carlo simulation is performed with the Geant4 toolkit, version 9.6.02. The particle interactions in matter are described in this work by means of the models listed in table 2. Additionally, the Doppler broadening and the photon polarization effects are included.

2.2. Beam structure

2.2.1. Beam structure measurements at HIT. Our group performed a set of measurements to characterize the beam time structure of the synchrotron installed in the Heidelberg Ion Therapy Center (HIT), Germany [Peters et al., 2008]. This set of measurements extends the results reported in [Peters et al., 2008] and is then used to reproduce a realistic beam in the simulation.

The beam characterization has been performed for 200 MeV/u and 400 MeV/u primary carbon ion energy with a two-fiber hodoscope (basic prototype of the one

currently under development) and the spill signal was given by the accelerator. Figure 2 shows the results for carbon ions at 400 MeV/u. The pulses have a spill period of 150.2 ns and each bunch is approximately 21.5 ns. The mentioned measurements have shown that the spill phase changes during the extraction: this implies that the HF signal from the synchrotron can not be used to trigger the pulses, so that the use of an additional beam time stamp system like the hodoscope seems required for time-of-flight background rejection purposes.
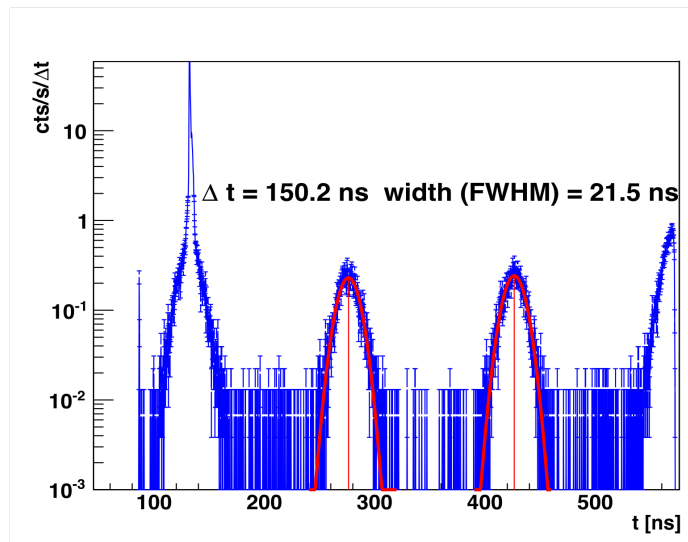

Figure 2: Beam time micro-structure measured from a carbon ion beam at 400 MeV/u delivered at HIT (time difference between two crossed-scintillating fibers). The offset between the two fibers is arbitrarily set to 130 ns. The pulses have an extraction period of 150.2 ns and the bunches are 21.5 ns FWHM. On the horizontal axis the time has been measured with a two-scintillating-fiber hodoscope, with 1 ns FWHM time resolution.

2.2.2. Beam modeling The two main beam particles used in clinics are considered in the simulation: protons and carbon ions. The beam range of interest is 15.2 cm in the PMMA phantom, and the associated energy is 160 MeV for protons and 305 MeV/u for carbon ions.

The beam transverse dimension is modeled with a Gaussian distribution with a standard deviation of 5 mm for protons at 160 MeV and 3.5 mm for carbon ions at 305 MeV/u. The number of incident ions for a spot in pencil beam scanning (PBS) mode is 10^8 for protons (distal spot - upper intensity limit) and 10^5 for carbon ions (average spot intensity) [Kramer and Scholz, 2000, Grevillot et al., 2011, Smeets et al., 2012]. In the simulation, the beam intensity is modeled by an average number of particles per bunch. The exact number of particles in each bunch is given by a random extraction from a Poisson distribution, where the mean value is the selected beam intensity.

The beam time structure is applied at the data analysis stage. Two different time

structures have been considered for this study, related to two kinds of accelerators used in clinical practice: the IBA C230 cyclotron for protons (used in 16 clinical centers worldwide) and the HIT synchrotron for carbon ions. For protons at 160 MeV, the primary particles are grouped in bunches of 2 ns (this value may vary also according to the distance between the cyclotron and the treatment room, and energy spread selection) at a frequency of 106 MHz (9.42 ns) [Roellinghoff et al., 2014]. The clinical beam intensity is 3.2 nA which corresponds to about 200 protons per bunch. Concerning the carbon ion beam at 305 MeV/u, the simulated time structure refers to the measurements presented in section 2.2.1. We used 30 ns duration bunches at a frequency of 5.9 MHz (170 ns period). The clinical beam intensity for carbon ions is 5×10^7 ions/s during extraction, corresponding to about 9 ions per bunch. The macro-structure (50% duty cycle with [1,5] ns period) is not considered.

The coincidence window (between scatterer and absorber singles) is set to 40 ns, centered on each absorber detected interaction. This value is adapted to the detectors time resolutions. At the simulation stage, each interaction in the detector layers is collected with the related local time. The beam time structure is then applied to each single hit, and the selected coincidence window is used to retrieve scatterer-absorber coincidence events, which are classified as described in section 2.3 in various types of true and random coincidences.Table 3 summarizes the presented beam time structures and coincidence reconstruction features.

Table 3: Description of the two beam structures studied: the IBA cyclotron C230 for protons and the synchrotron installed at the Heidelberg Ion Therapy Center (HIT) in Germany for carbon ions. The macro-structure of the synchrotron, at the second time scale, is not considered here. The beam structures are applied to the simulation data.

		Protons	**Carbon ions**
Clinical features	Facility	IBA Cyclotron C230	Synchrotron at HIT
	Clinical intensity	2×10^{10} p/s	5×10^7 ions/s
	Energy	160 MeV	305 MeV/u
Beam structure	Bunch time [ns]	3.2	30
	Period [ns]	9.4	170
	Primaries/bunch	217	9
Detectors	Coincidence window [ns]	40	40
	Time resolution (FWHM) [ns]	Si: 15 and BGO: 3	

2.3. Compton camera events

The Compton detection principle is based on the time coincidence of at least one scatterer and one absorber gamma interaction, where an interaction is defined as an energy deposit in a detector module, with the spatial selections detailed in section 2.1. As discussed in section 2.2, the coincidence reconstruction relies on a defined time window, fixed according to the detector resolution. In a simulation environment, different kinds of coincidence events can be distinguished and studied:
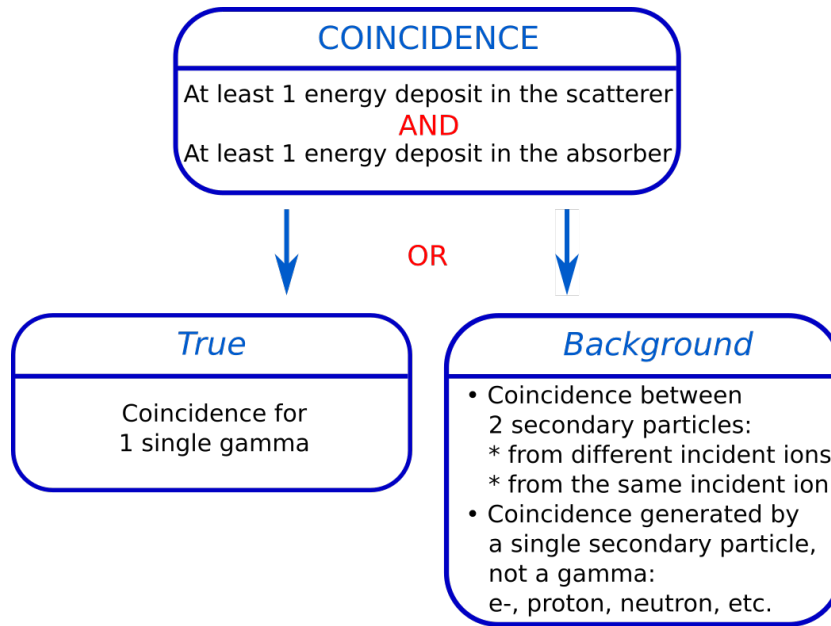
Figure 3: Diagram showing the different definitions of coincidences in the Compton camera. The energy deposits are selected in the silicon scatterer to be limited to neighboring strips (3 strips maximum), and in the absorber blocks the events are selected to be limited to a single block.

- true coincidences, created by a single photon interacting in the scatterer stack and in the absorber block array;
- quasi-simultaneous interaction of two secondary particles (photons – random coincidences – or massive particles), from the same incident ion of from different incident ions;
- double interaction of the same particle, not a photon (e.g. protons, neutrons).

A scheme representing the different kinds of Compton camera events is sketched in Figure 3. All the coincidence events that are not true coincidences contribute to the signal background, and will be referred to background coincidences in the following.

Also in the single detector sections, different kinds of events can be identified in a simulation environment. As described in section 2.1, the simulation setup selects events with absorber interactions limited to a single BGO block. Focusing on the scatterer section, among the true coincidences, three different kinds of events can be identified:

- gamma undergoing one or more interactions in a single silicon layer, with no other layers hit;
- gamma undergoing interactions in more than one silicon layer;
- Compton electron escape events: gamma undergoing Compton interaction in one layer and providing enough energy to the recoil electron to make it escape the layer where it has been created and interact in one or more of the next ones.

As mentioned in the introduction, events involving more than one photon interaction in the scatterer layers are advantageous since the total absorption of the detected prompt gamma is not required to reconstruct the Compton cone. However, the actual selection of such kind of true coincidence events with respect to background interactions in real conditions is hardly achievable. Anyway, as it will be shown in section 3.1, the amount of these events with respect to events with a single interaction in the scatterer stack is negligible.

On the other hand, electron escape events can be in principle identified and exploited. They are characterized by two or more scatterer layers involved: if the first Compton interaction in one layer provides enough energy to the recoil electron, it can escape the silicon plane and be detected by one (or more), neighboring planes. Thus, such events can be identified by the electron tracking, and carry additional information with respect to a Compton interaction with no electron escape. The electron tracking allows to reduce the reconstructed Compton cone to an arch of the cone, by the overlap of the cone with the electron tracking plane.

2.4. TOF and energy based data selection

Experimental data contain a certain number of the background coincidences (see Figure 4), which cannot be distinguished from true coincidences. Such a background level depends on the detector time resolutions, the fixed time coincidence window and the beam time structure, the phantom composition and the camera prototype setup. *Ad hoc* filtering methods are applied to reduce the above described contamination.

- Time-Of-Flight (TOF): it has been demonstrated that a time-of-flight discrimination is possible and effective in reducing the background generated by massive particles interactions [Testa et al., 2010]. The massive particles approach the detector at a lower speed with respect to photons. The time information provided by the hodoscope and the absorber can be combined to fix a detection time window and reject all the events outside the window. The time elapsed between the incident particle detection in the hodoscope and the secondary particle detection in the absorber is considered as the time-of-flight. In order to define the appropriate time window, the TOF spectra of the collected events resulting from the irradiation of the PMMA target with 10^8 160 MeV protons have been produced for true gamma coincidences and background events, taking into account the detector resolutions. The result is shown in Figure 4. For this study, no time structure has been applied to the primary protons, thus only independent events have been considered. The time-of-flight spectrum resulting from the simulation shows that:
  - the coincidences of interest (produced by prompt-gamma rays) are included in a window between 0 and 8 ns;
  - in the TOF window a comparable amount of true coincidences and background events is observed. Since we consider only independent events, this means that such background events are due to random coincidences between two
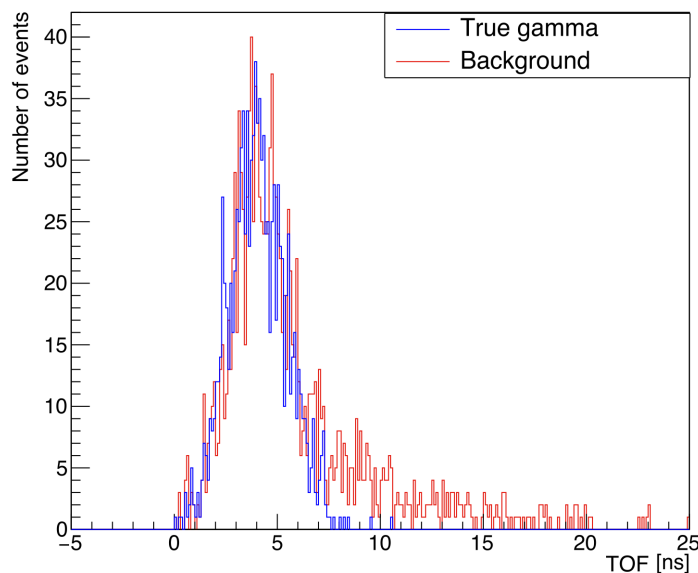
Figure 4: Time of flight spectra of true gamma coincidences (blue) and background events (red) obtained with 10^8 160 MeV independent incident protons.

> prompt gammas directly or indirectly induced by the same incident ion. The background events outside the TOF window are due to massive particle interactions in the camera.

It is worth to stress that the simulation results shown in Figure 4 do not include random coincidences, created by prompt photons emitted by different primary ion interactions, and room background, mainly due to neutrons. Both components contribute to the background spectrum. In the case of the C230 cyclotron accelerator, the room background has been measured and showed a flat distribution in time [Pinto et al., 2014]. When the beam time structure is applied to the simulated data (including the detector time resolutions), the lists of time-ordered interactions in hodoscope and absorber are produced. For each coincidence events, we look for the first hodoscope event in the 8 ns time window preceding the absorber interaction time. All events with no hodoscope coincidence in the time window are rejected.

- Energy selection: energy thresholds are defined for the event detection. 50 keV and 100 keV are set as lower threshold for the energy deposited in a single silicon layer and BGO block, respectively. For a complete event, a total absorbed energy lower limit is set to 1 MeV. In addition to the effect of background rejection, this selection also reduces the impact of partially absorbed photons.
  Further energy selections, assuming for instance $E_1 + E_2$ equal to one of the strong gamma lines, have been applied by other authors [Draeger et al., 2017]. Also, filters checking the possibility of reconstructing a Compton cone could be used. At this stage we did not consider such approaches in order to cope with simple

considerations on signal to noise on raw data.

2.5. Reconstruction algorithms

Once the coincidences are defined and selected according to the fixed physical cuts, the prompt-gamma emission distribution has to be reconstructed. This can be done via analytic or iterative algorithms based on the Compton kinematics. Both are presented in the following sections.

2.5.1. Line-cone algorithm. The reconstruction via line-cone algorithm exploits the energy deposit and position information collected by the camera in addition to the beam spatial information provided by the hodoscope. Thanks to the deposited energies in the detectors and the interaction positions, a cone surface is analytically defined via the Compton equation 1. Figure 5 shows a sketch of the reconstruction principle. The interaction position in the scatterer gives the cone apex and the line connecting the interaction positions in scatterer and absorber gives the cone axis. We assume that the initial energy of the gamma ray is fully absorbed in the absorber. This assumption has been investigated and the results are shown in section 3.2. In order to constrain the reconstruction, the beam direction is used to limit the possible solutions (lying on the reconstructed cone surface) to two points (intersection of the beam direction and the reconstructed cone). At this stage we do not consider the lateral beam spread in the target, due to multiple scattering. The set of all the reconstructed points gives the emission source distribution. The final image is the mono-dimensional projection of the prompt gamma emission profile, and each bin of the profile follows a Poisson statistics.

2.5.2. LM-MLEM algorithm. The iterative methods allow to get a 3D image reconstruction, potentially by taking into account the spatial and the energy resolutions of the detectors. Several iterative algorithms have been developed for Compton image reconstruction [Wilderman et al., 1998, Schone et al., 2010, Andreyev et al., 2011, Zoglauer et al., 2011, Gillam et al., 2011, Mackin et al., 2012, Lojacono et al., 2013, Taya et al., 2017, Schoene et al., 2017, Huang et al., 2018].

The *List-Mode Maximum Likelihood Expectation Maximization* (LM-MLEM) algorithm is a MLEM version which enables one to reconstruct the image directly from the list of detected events. The obtained distribution, as opposite to the line-cone reconstruction, does not show a Poisson behavior. The features of the LM-MLEM algorithm used for this study are detailed in [Hilaire et al., 2014].

2.6. Performance study

In this section the factors studied to assess the camera performance are explained. The study is mainly divided into four sections:
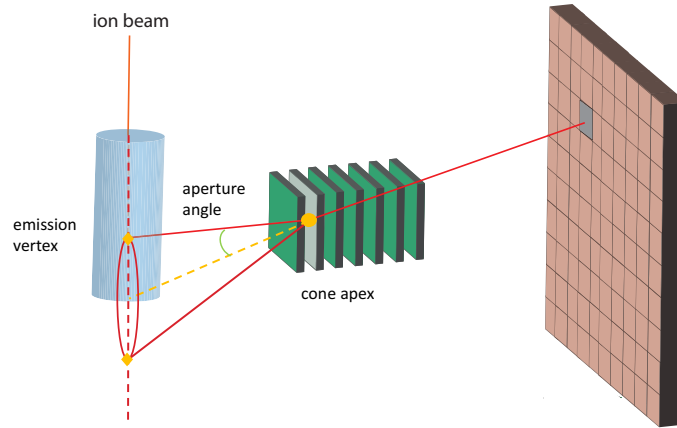
Figure 5: Scheme of the line-cone reconstruction method. Two points are extracted for each event (diamonds in the figure), provided by the intersection between the reconstructed Compton cone and the beam line. The result is a mono-dimensional profile.

- the detection efficiency of the various types of true coincidences defined in section 2.3 is studied by means of mono-energetic irradiation with point-like sources as a function of the incident gamma energy;

- the absolute camera efficiency for the detection of events with a single scatterer layer involved is studied by means of mono-energetic irradiation with point-like sources as a function of the incident gamma energy and the source position with respect to the camera. The absolute efficiency is defined as the ratio between the number of selected true coincidences and the total number of emitted gammas (see equation 2.6.2);

- the rate of background coincidences (for events with a single scatterer layer involved) is studied as a function of the beam intensity, with proton and carbon beams impinging on the PMMA phantom;

- the camera precision, defined as its capability of identifying the fall-off of the prompt-gamma emission profile, is tested (for events with a single scatterer layer involved) with the analytic line-cone and the iterative LM-MLEM reconstruction algorithms.

2.6.1. Detection efficiency of various types of true coincidences   The efficiency is crucial for the Compton camera performances and for its possible application in treatment monitoring. An efficient monitoring system should be ideally in real time, in order to allow for a treatment adaptation or interruption in case of severe issues detected in the delivered dose profile with respect to the planned treatment. In order to achieve an online detection of such deviations, given the limited prompt gamma emission rate per

incident ion [Ortega et al., 2015], a high detection efficiency is required to perform a monitoring on, ideally, a beam spot basis. In addition to this, the absolute detection efficiency directly affects the image reconstruction quality, which is in general increased for increased statistics.

The efficiency in the detection of various kinds of true coincidence events, with specific interaction patterns in the scatterer section, detailed in section 2.3, has been studied with the irradiation from point-like mono-energetic gamma sources. The setup is the same as Figure 1, with the exception of the PMMA phantom which is removed to leave the gamma source in air. Different energies have been tested to mimic different prompt gamma lines: 300 keV, 500 keV, 1 MeV, 2 MeV, 4 MeV, 6 MeV. No time structure is reproduced for this part of the study. In addition, the rate of events with an almost full primary energy absorption has been studied for the various kinds of coincidences as a function of the primary gamma energy. The threshold for the energy absorption has been set to 90% of the primary gamma energy. The results of this preliminary study (see section 3.2) determined the choice to limit the next investigations to events with a single scatterer plane involved; all events with more than one scatterer layer hit have been rejected for the analysis described from section 2.6.2 and the results presented from section 3.2.

2.6.2. Absolute detection efficiency The absolute efficiency ϵ for the detection of coincidences with a single scatterer plane hit is defined as:

$$\epsilon = \frac{N\gamma_{\text{coinc}}}{N\gamma_{\text{total}}}, \tag{3}$$

with $N\gamma_{\text{coinc}}$ the number of gamma events corresponding to the selected true coincidences, $N\gamma_{\text{total}}$ the total number of emitted gammas.

In addition to its dependence on the gamma energy in the range 300 keV – 6 MeV (see section 2.6.1), the absolute efficiency has been also studied as a function of the point-like source position. The source is set in the range -300 mm to $+300$ mm (with the center of the camera transverse section set in the position 0), and moved with variable length steps, up to 1 cm. The movement followed the transverse axis of the camera.

2.6.3. Rate of background coincidences As the Compton detection principle relies on time coincidences, in addition to the main importance played by the detectors energy resolutions, the beam intensity and time structure are important parameters to be studied in order to assess the possible clinical implementation of a Compton detection based monitoring of ion beam treatment. The ability of the detection system to distinguish between true and background coincidences, i.e. the resulting signal over noise ratio, strongly depends on the beam time structure. The number of true and background coincidences is studied as a function of the beam intensity, before and after data reconstruction via line-cone algorithm (see section 2.5). To be noticed that,

following the results of the efficiency study (see section 3.2), only events with one single scatterer layer hit are selected.

The range of intensities is defined in order to cover a wide range of operation: from a very low beam intensity to a realistic clinical particle rate. Therefore, for proton and carbon ions, the lowest beam intensity is set to 0.1 particles per bunch on average, while the upper limit is set to 217 protons or 70 carbon ions per bunch. All the simulations are performed with a total of 10^8 primary protons and 2×10^5 primary carbon ions (see section 2.2.2).

2.6.4. Camera precision The camera precision is defined as the difference between the predicted PG fall-off position - FOP - (according to the treatment planning) and the detected one. It is studied with proton beams. A preliminary reconstruction test is performed with the two algorithms (line-cone and LM-MLEM) and 10^8 incident protons, at two beam intensities: the clinical intensity – 200 protons per bunch – and a reduced intensity of 1 proton per bunch. For the LM-MLEM reconstruction, the volume is set to $20 \times 40 \times 1$ cm^3 around the expected FOP, with a $101 \times 201 \times 5$ voxel matrix. To be noticed that the two reconstruction methods produce different results: the line-cone method is based on the beam direction information, so that it naturally returns a mono-dimensional profile as result, while the LM-MLEM method is able to reconstruct the PG emission distribution in three dimensions. A mono-dimensional projection along the beam direction is used for the fall-off identification and for a direct comparison with the line-cone method. As a result of this preliminary evaluation (see section 3.4), the camera precision is evaluated with a beam intensity of 1 proton per bunch, with the analysis described in the following paragraphs.

A reference profile is defined for each reconstruction method as the reconstructed (line-cone or LM-MLEM) distribution of emission positions at high statistics (2×10^{10} incident protons). The *SmoothKern* method, with the Nadaraya-Watson regression [Nadaraya, 1964, Watson, 1964], is used to smooth the reference profiles in order to reduce relative statistical fluctuations. A ROI ranging from $y = 0$ mm to $y = +100$ mm is defined around the expected FOP, located at $y = +50$ mm in the phantom. The reference profiles are modeled in the ROI by a linear combination of Non-Uniform Rational Basis Splines (NURBS) [Rogers, 2001]. The retrieved FOPs are used as reference and compared to the ones obtained for lower numbers of incident primaries, in the range 1×10^8 to 5×10^9. The data selected for the reference profiles are divided into subsets with random extractions. The number of events composing each subset is selected according to the desired incident proton statistics (considering the total amount of data collected for 2×10^{10} incident protons), and a statistical fluctuation is added with a random extraction from a Gaussian distribution centered in the defined statistics. For each number of incident primaries, 100 data subsets are extracted with this method and reconstructed with the line-cone and LM-MLEM algorithms. To be noticed that for the LM-MLEM algorithm, a preliminary study has been necessary to define the optimal reconstruction parameters, in particular the number of iterations required. The

iterative algorithm, indeed, tends to concentrate the reconstructed emission map in "hot-spots", creating artifacts which bias the precision evaluation. This effect is all the more significant at low statistics. The reconstructed profiles have been studied for a number of algorithm iterations ranging from 1 to 20, and for four incident proton equivalent statistics. The results presented in section 3.4 determined the choice of selecting the profiles after two iterations as the optimal trade-off to implement a common method for the precision evaluation in the whole explored primary statistics range. For what concerns the reconstructed volume, two configurations have been tested: $20 \times 40 \times 1$ cm^3, with a $101 \times 201 \times 5$ voxel matrix, and $20 \times 40 \times 10$ cm^3, with a $101 \times 201 \times 50$ voxel matrix. In the second case, a 1 cm slice in the direction perpendicular to the camera entrance surface (z in Figure 1) has been selected after reconstruction to compare the two configurations. No significant differences emerged from this test, so that the 1 cm volume extension in the perpendicular direction, with 5 voxels, has been chosen to avoid the loss of statistics determined by the larger reconstruction volume.

Once all the low statistics profiles are obtained for the two reconstruction methods, a custom minimization technique is applied to deduce the minimal shift between the reference profile and the one at lower statistics. The minimization algorithm shifts the reference profile in a 60 mm range, between -30 mm and $+30$ mm with respect to the initial position, with a step of 1 mm. For each step, the reference profile is compared (bin by bin) to the low statistics profile by calculating the χ^2 as follows:

$$\chi^2 = \sum_{i=1}^{N_{bin}} \left(y_{\text{sample,i}} - y_{\text{NURBS,i}}\right)^2, \tag{4}$$

where for every bin i, y_{sample} is the number of events in the low statistics profile, y_{NURBS} is the number of events for the reference profile NURBS (scaled at the same low statistic). The described approach is robust and allows to avoid artifacts at low statistics. The global minimum of all the calculated χ^2 is then retrieved and the shift associated to this value is added to the shift distributions. The standard deviation of the distribution gives the precision of the camera for a given number of incident protons.

3. Results

The possible implementation of the CLaRyS Compton camera as a monitoring system for ion beam therapy has been investigated. The camera has been exposed to point-like gamma sources to study the detection efficiency. A PMMA cylindrical phantom has been simulated and exposed to proton and carbon beams at increasing intensities for an analysis of the prompt gamma detection environment (background, random coincidence contamination). The camera precision in the identification of the fall-off of the prompt gamma emission profile has been investigated. In the following sections we show the obtained results.

3.1. Detection efficiency of various types of true coincidences

Figure 6 shows the Compton camera efficiency in detecting the kinds of coincidence events described in section 2.3, as a function of the gamma energy in the prompt-gamma energy range (between 300 keV and 6 MeV). The results show how the single events, consisting in the coincidence between an energy deposit in a single scatterer layer and in one single absorber block, decreases at increasing energy, in favor of an increase in the number of electron escape events (consisting in one primary photon Compton interaction in one scatterer layer, at least one interaction of the Compton escaped recoil electron in a different scatterer layer, and one primary photon interaction in one single absorber block). At the maximum investigated primary gamma energy, the amount of electron escape collected events is more than 35%. However, the single events represent more than 60% of the total amount of collected events in all the explored energy range, so that the results in the following paragraphs are focused on this kind of events (with the other kinds of events rejected at the analysis stage), as first approach for a feasibility study. The amount of 3 or more photon-interaction events is limited and negligible over the whole energy range.
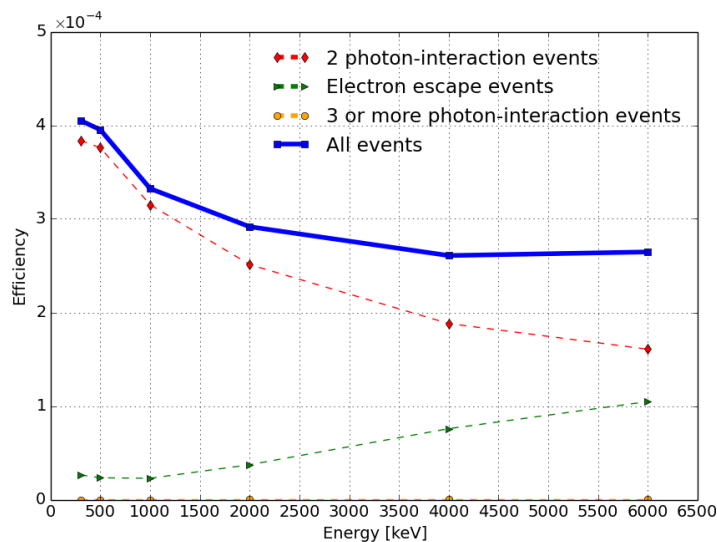

Figure 6: Compton camera efficiency as a function of the gamma energy for the different kind of possible coincidence events (see section 2.3), as a function of the gamma energy.

Figure 7 shows the rate of events with more than 90% of the primary gamma energy deposited in the detector layers. The rate of 90% absorbed events is reported for the different kinds of detected coincidences. As expected, the rate of almost fully absorbed events decreases as the energy increases, in a range between more than 80% and 40% for 300 keV and 6 MeV primary photon energy, respectively. The most of the 90% absorbed events are single events, with the electron escape and multiple ones negligible for primary gamma energies above 1 MeV. At lower energy, the Compton recoil electron is often able to exit the scatterer layer where the Compton interaction takes place, but
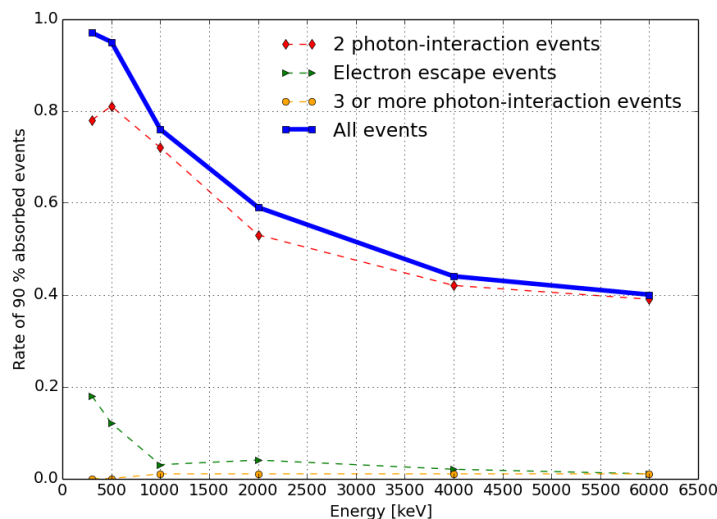
Figure 7: Ratio between coincidence events with more than 90% of the primary photon energy absorbed in the detector layer and all detected coincidences as a function of the gamma energy. The curves shown the results for the different kind of possible coincidence events and for the all collected coincidences.

can be lost without further interactions, so that this kind of events is considered as single with an energy absorption below 90%. This can explain the decrease of single almost full absorption at 300 keV. If the electron interacts with a scatterer layer, it is generally absorbed at low energy, explaining the increasing electron escape absorbed events below 1 MeV. As mentioned, these results led to the choice of limiting the further analysis (from section 3.2) to events with a single scatterer layer involved, as first approach.

3.2. Absolute detection efficiency

Figure 8 shows the absolute gamma detection efficiency as a function of the gamma source position with respect to the center of the camera in the transverse plane. On the left side, we show the results achieved without energy detection thresholds. On the right side realistic energy thresholds are applied on each detector section (50 keV for the scatterer layers and 100 keV for the absorber).

As expected according to the interaction probability energy dependency, the efficiency is higher for low gamma energies, and it lies in the range 4×10^{-4} at 300 keV and 1.5×10^{-4} at 6 MeV at the center of the camera. Moreover, it can be noticed how the efficiency drops as the point source is shifted away from the camera center: efficiency reductions of a factor approximately 4 and 8 at 500 keV and 4 MeV, respectively, are detected with the source at 300 mm distance from the camera center, with respect to the value detected in central position. This effect is more important for high energies, for which the incident gamma is less deflected in the scatterer for the same energy deposited compared to a low energy gamma. Figure 8(b) shows the effect of realistic camera detection thresholds as opposed to the detection without energy thresholds. The
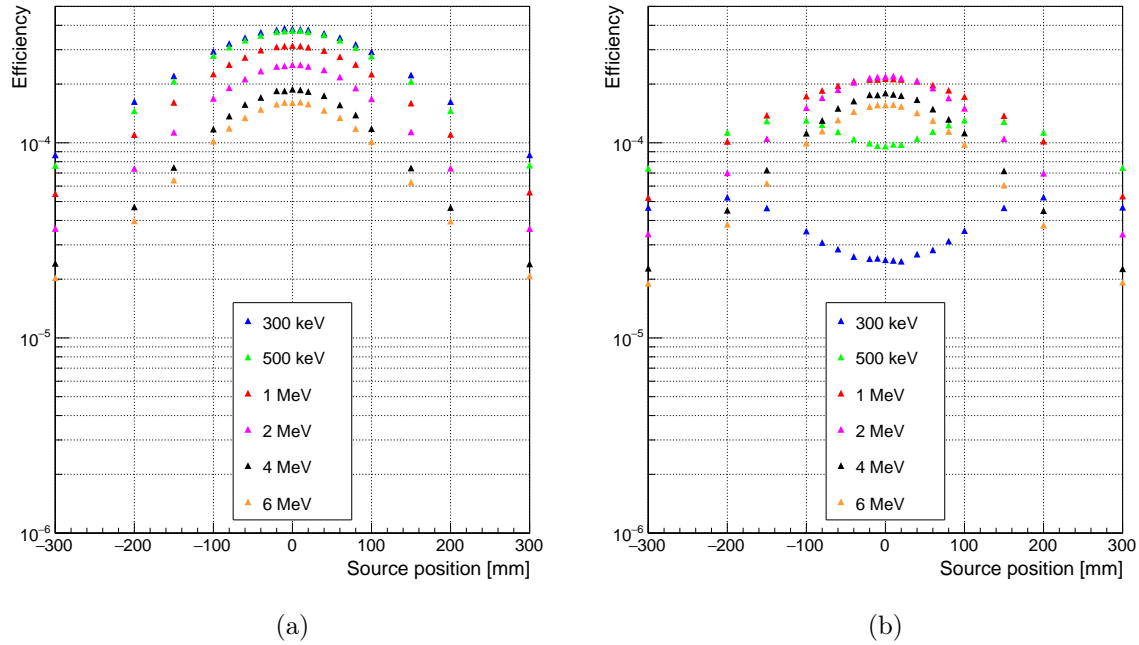
Figure 8: Absolute Compton camera efficiency as a function of the gamma source position for different gamma energies, in the range between 300 keV to 6 MeV. The left side shows the camera efficiency with no detection energy threshold. In the right side, detection energy thresholds are applied to reproduce a realistic scenario (lower limit of 50 keV for the scatterer, 100 keV for the absorber). These values can change for the final configuration, according to the detector energy resolutions achieved.

gamma detection efficiency drops of a factor ranging from about 1.25 to more than an order of magnitude for the central detection area for energies in the range 300 keV to 2 MeV respectively. The effect is reduced by the distance of the source from the center of the camera. Negligible effects are detected for positions with a distance greater than 200 mm from the center of the camera, and for any distance at energies above 2 MeV, while the efficiency is reduced in the central area of the camera for energies below 4 MeV.

3.3. Rate of background coincidences

In Figure 9, the different components of the signal resulting from the PMMA exposure to proton and carbon ion beams are shown as a function of the beam intensity. The true coincidences represent scatterer-absorber time coincidences generated by the same gamma ray (only events with hits in a single scatterer layer). All the other coincidence types compose the background. The collected data sets are reported with and without the applied time-of-flight discrimination, mainly employed for neutron rejection, as mentioned in section 2.4.
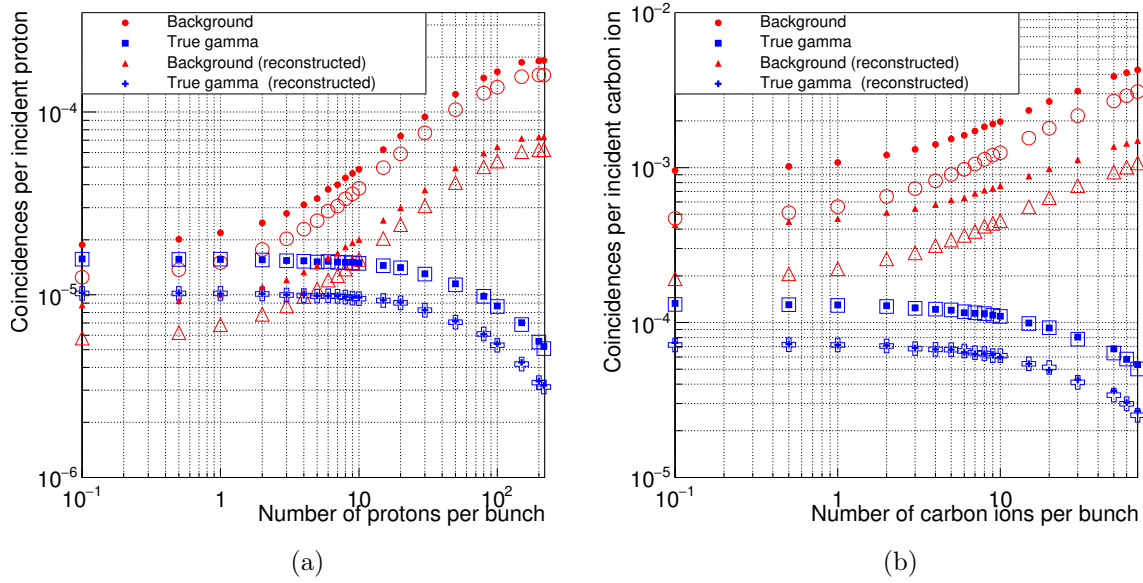
Figure 9: Coincidences yield for protons (left) and carbon ions (right) as a function of the beam intensity. The intensity is reported as number of incident particles per bunch. The filled markers correspond to the collected data without time-of-flight discrimination, while this cut is applied to the data reported with empty markers. Moreover, the yields are given before and after the profile reconstruction with the line-cone algorithm, which rejects events reconstructed out of the target volume.

In Figure 9(a) and (b) the amount of true gamma coincidences and background events are reported before and after reconstruction via line-cone algorithm as a function of the beam intensity for proton (a) and carbon ion (b) beams. In addition to this, for each curve realized with the complete collected data set, the related one obtained after time-of-flight selection of events is sketched (empty symbols). All the curves have been normalized to the number of incident ions.

The amount of background events (mainly random coincidences - due to quasi-simultaneous interactions of different gammas) increases with the increasing beam intensity: a factor of about 30 with respect to true gamma events is obtained for proton beams at the intensity of 200 protons per bunch with no event selection, while a factor more than two times higher is reported for carbon ions in the same conditions. The time-of-flight selection can slightly improve the signal-to-noise ratio by reducing the amount of background events. The amount of true gamma events and background events becomes similar at the intensity of about 1 proton per bunch. As expected by the observation of Figure 4, for intensity values below 1 proton per bunch, the ratio between true and background events remains stable.

3.4. Camera precision

The camera precision in the fall-off identification is investigated with proton beams. A data set corresponding to the irradiation of the PMMA phantom with a monoenergetic 160 MeV proton beam spot (10^8 protons) has been collected and analyzed with a clinical intensity of 200 protons per bunch and a reduced one with 1 proton per bunch on average. Figure 10 shows the results of the line-cone and LM-MLEM reconstructions of the simulated data for the two beam time structures applied at the analysis stage.

The results obtained for a clinical intensity of 200 protons per bunch qualitatively show how the fall-off of the prompt-gamma profile cannot be retrieved with the two applied reconstruction methods, due to the contamination of background events. The fall-off can be identified at the reduced intensity of 1 proton per bunch for both line-cone and LM-MLEM reconstructed data. For this reason, the camera precision is studied at the reduced intensity of 1 proton per bunch on average, at which a comparable rate of true and background events is expected, following the results shown in section 3.3.

Figure 11 shows the PG profiles obtained for four incident proton statistics in the explored range (10^8, 5×10^8, 10^9, 5×10^9), reconstructed with the LM-MLEM iterative algorithm, for different numbers of iterations, in the range [1,20].

The presented profiles show the effect of the increasing number of iterations of the reconstruction algorithm, which tends to concentrate the emission vertexes in "hot-spots" creating artifacts which bias the identification of the profile fall-off, mainly at the lowest explored primary statistics. The profile fall-off can be identified with minimized artifacts after 2 iterations of the LM-MLEM algorithm. For this reason, 2 iterations are used for the precision study.

A total of 2×10^{10} protons has been simulated to define the reference PG profile, with a beam intensity of 1 proton per bunch on average, and then different low statistics profiles have been produced for the precision estimate as explained in section 2.6.4 for both the line-cone and the LM-MLEM reconstructions. The high statistics profile reconstructed via line-cone algorithm is shown in Figure 12a and via the LM-MLEM reconstruction method in Figure 12b with the related NURBS fit. A NURBS fit of a low statistics sample (10^8 incident protons) is shown in Figures 12c for the line-cone and 12d for the LM-MLEM. Poisson extracted fluctuations have been added to the fit curve in the range 30-70 mm (where the fall-off position is expected to be located) for the line-cone case, while the low statistic profile for the LM-MLEM case is obtained with the extraction of a data subset from the reference profile data set and shown together with the reference profile related NURBS. The retrieved optimal shift distribution is shown in Figure 13a and 13b for the line-cone and LM-MLEM algorithm respectively, for 10^8 incident protons as well.

The analysis method described in section 2.6.4 is applied to the different PG obtained profiles to retrieve the camera precision in the fall-off identification. The results are shown in Figure 14, where the two reconstruction methods are represented by different markers.
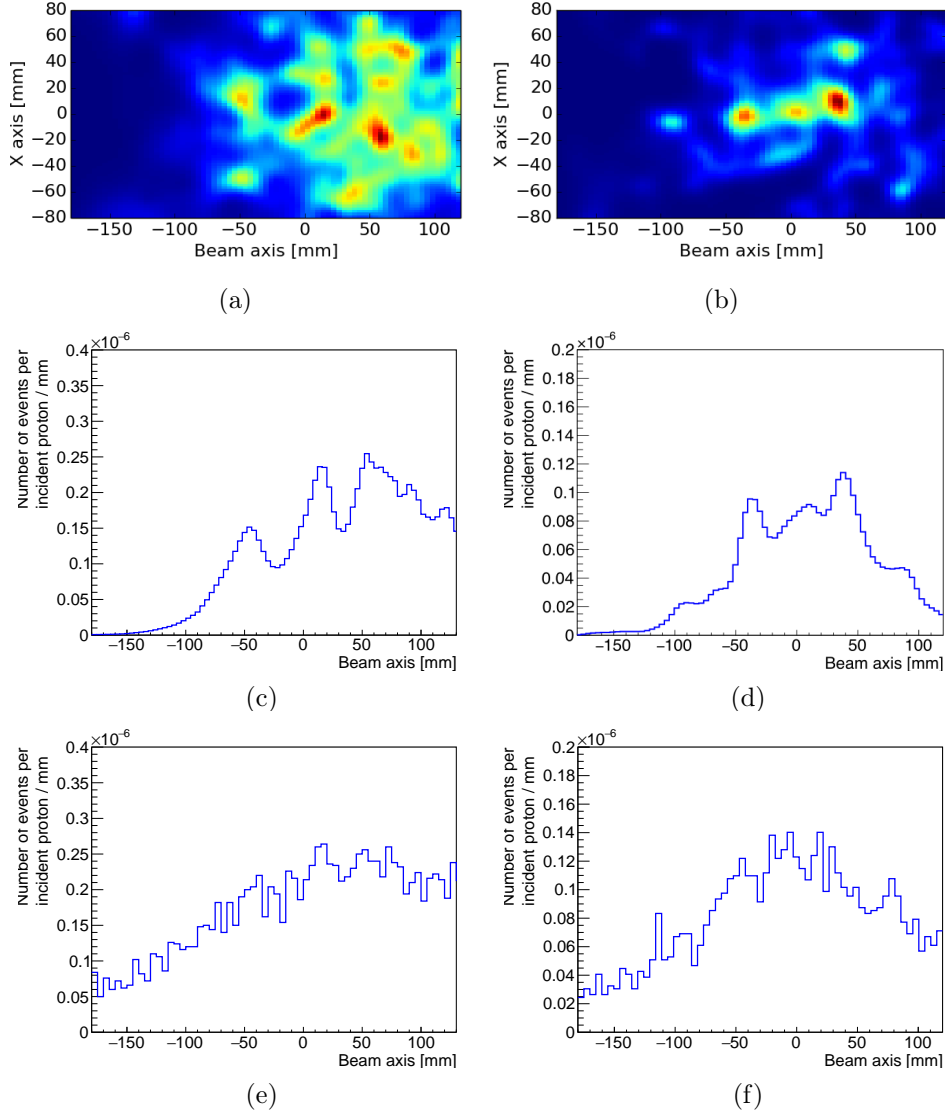
Figure 10: Line-cone and LM-MLEM reconstruction for a 160 MeV proton beam, 10^8 total incident protons. In the left column, the beam intensity is 200 proton per bunch on average; in the right one, the beam intensity is 1 proton per bunch on average. The Compton camera is centered at the expected Bragg peak position, $y = +50\,\text{mm}$. The time-of-flight event selection is applied on the collected data set. 2 iterations are performed for the LM-MLEM reconstruction. The top row shows the MLEM reconstructed 2D images in the plane (x, y), parallel to the camera entrance surface. The position $x = 0\,\text{mm}$ corresponds to the center of the PMMA phantom and the y direction corresponds to the beam axis, with the target entrance at $y = -100\,\text{mm}$ and the target end at $y = +100\,\text{mm}$. The center row shows the 1D profiles along the y axis. The expected profile fall-off is located at $y = +50\,\text{mm}$. The bottom row shows the profiles obtained by means of the line-cone algorithm for the same time-of-flight selected data.
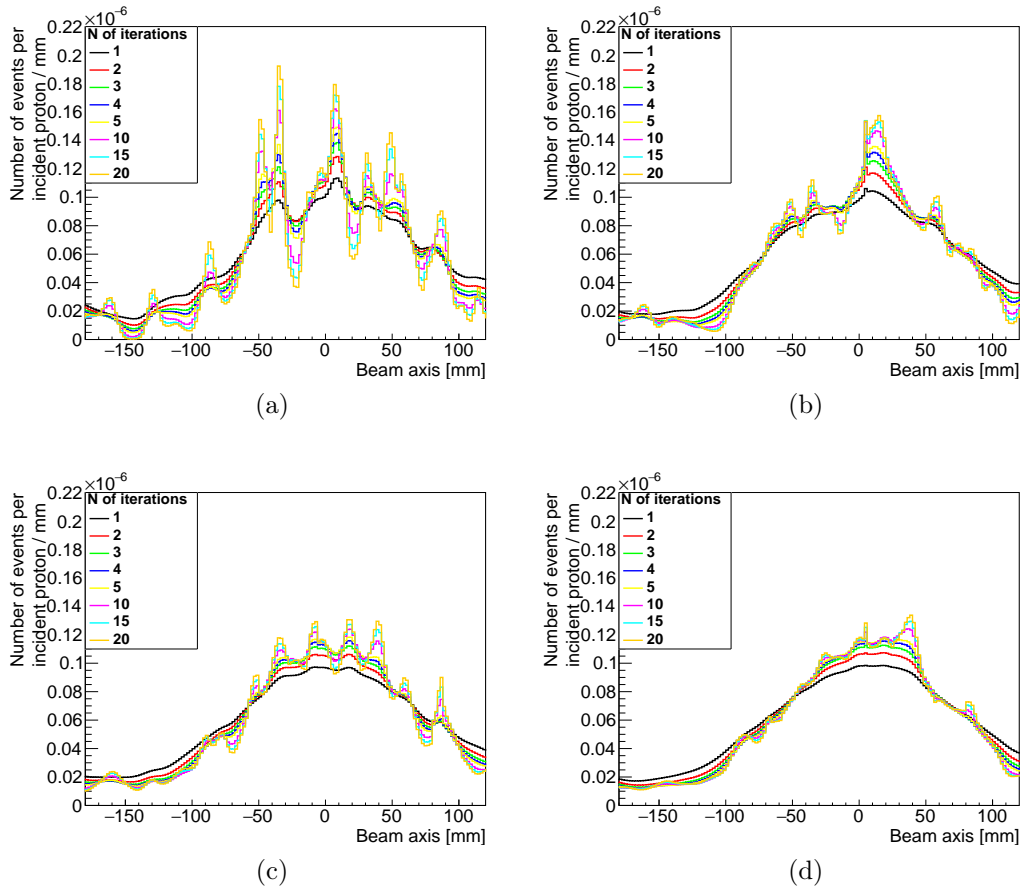
Figure 11: PG profiles for 10^8 (a), 5×10^8 (b), 10^9 (c), and 5×10^9 (d) incident protons reconstructed with the LM-MLEM algorithm, for 1, 2, 3, 4, 5, 10, 15, 20 iterations.

The iterative MLEM reconstruction method enables one to achieve a better precision with respect to the line-cone algorithm: the fall-off retrieval precision (FRP) is improved by a factor between 2.6 and 5 in the whole range of statistics explored. A linear behavior, highlighted by the performed linear fit of the two data sets, is verified with increasing number of primary protons, starting from the single spot scale of about 10^8 primaries, till 5×10^9 protons, which can correspond to the monitoring of a group of spots with the same planned range.
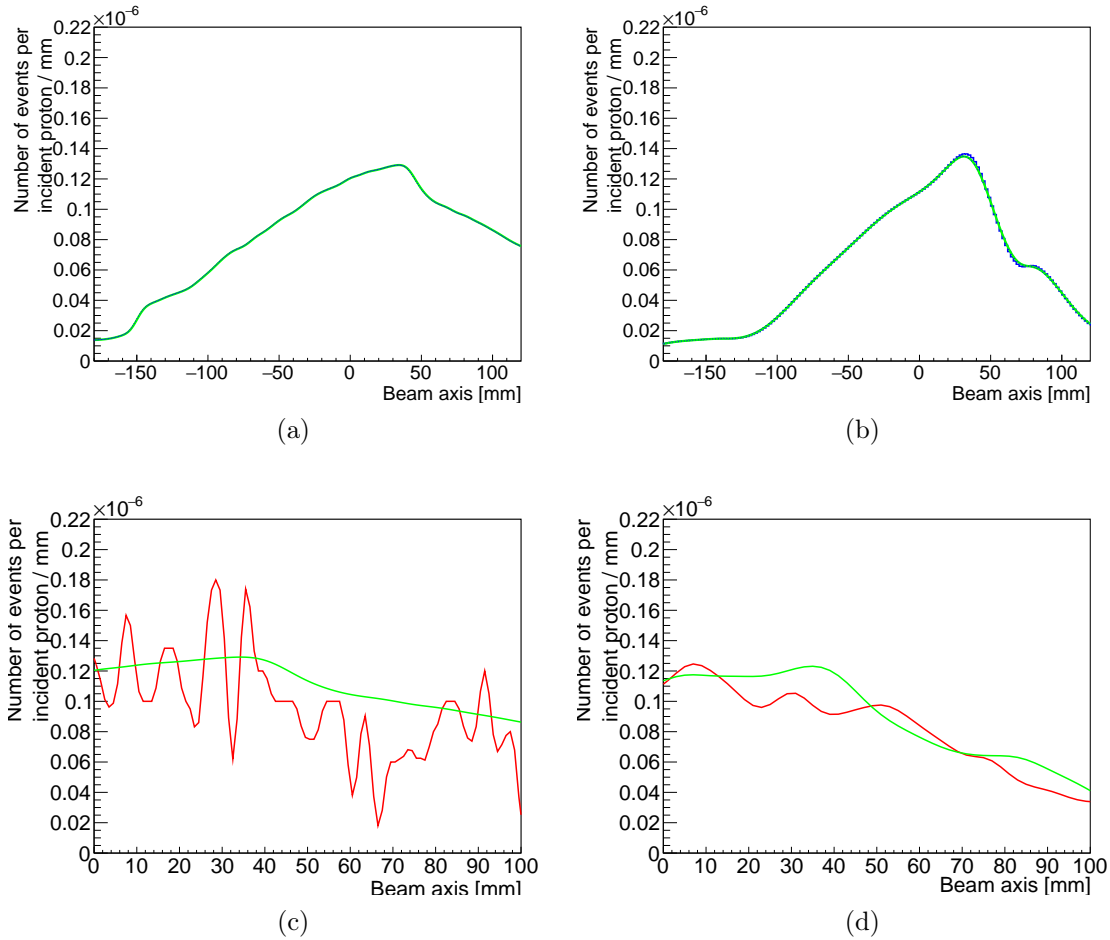
Figure 12: Top row: line-cone (a) and LM-MLEM (b) reconstructed reference profile (blue histogram) for 2×10^{10} incident protons, at a beam intensity of 1 proton per bunch, with the NURBS related curves (green solid lines). Bottom row: NURBS curve (green) obtained after the normalization to a 10^8 incident protons statistics, and Poisson generated statistical fluctuations (red) in the expected fall-off region, for the line-cone precision evaluation method (c), and profile realization for the LM-MLEM precision analysis (red – d) obtained with the reconstruction of a data subset (for 10^8 incident protons) extracted from the reference profile data set.

4. Discussion

We studied in this simulation work the performance of the CLaRyS Compton camera prototype and its possible implementation as prompt-gamma detector for ion beam therapy monitoring. The proposed analysis is focused on four main points: detection efficiency for various kind of coincidence events, and for events with a single scatterer layer hit absolute gamma detection efficiency, true and background coincidence rate and camera precision in the identification of the prompt-gamma emission profile fall-off.

The gamma detection efficiency has been measured with the detector exposed to

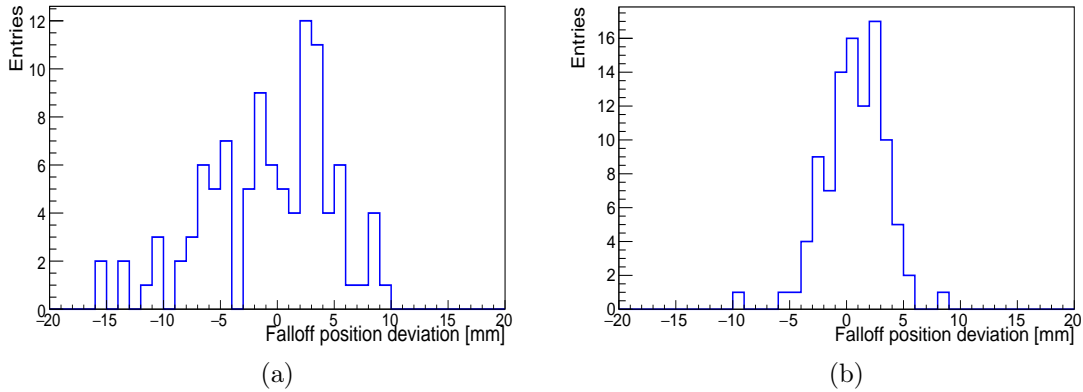(a)   (b)

Figure 13: Distributions of the fall-off position deviation with respect to the fall-off position of the high statistics reference profile for 1000 realizations with 10^8 primary protons obtained with line-cone reconstruction (left) and for 100 realizations with 10^8 primary protons obtained with the LM-MLEM reconstruction (right). The standard deviation of these distributions represents the Compton camera precision for the selected statistics.
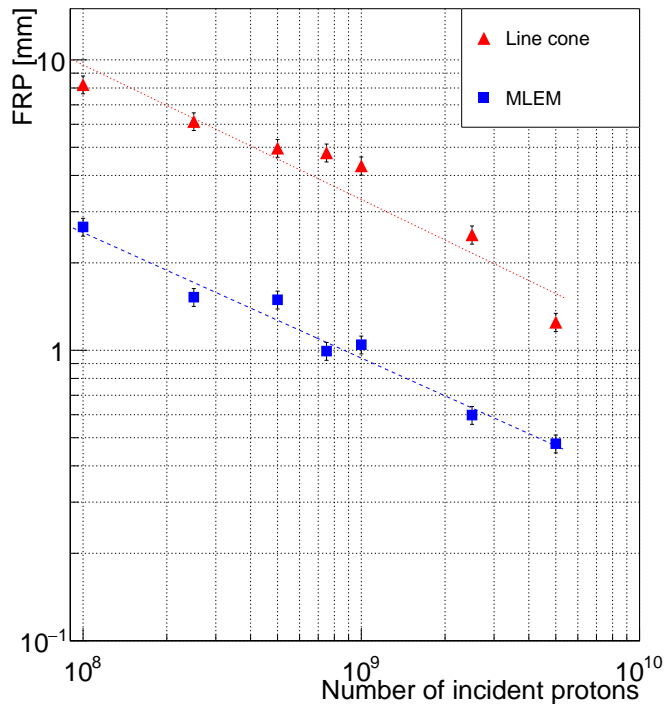

Figure 14: Fall-off retrieval precision (FRP) for two different reconstruction algorithms: line-cone and LM-MLEM. The precision is shown as a function of the total number of incident protons, in the range $[10^8, 5 \times 10^9]$.

gamma sources at six different energies, in the prompt-gamma energy range. The relative detection efficiency has been studied considering the three possible kinds of true coincidence events: single Compton interactions in the scatterer (2 photon interaction events), Compton recoil electron escape events and events with multiple gamma interactions in the scatterer (3 or more photon-interaction events). The coincidences composed of one single Compton interaction in one of the scatterer layers and an energy deposit in one single absorber blocks represent the majority of the collected events in the whole explored energy range. However, for energies above 1 MeV the amount of electron escape events becomes significant. Such kind of events can be ideally exploited in the reconstruction, and the selection can be based on tracking analysis (if the escaped recoil electron interacts in more than one scatterer layer). In the camera performance evaluation study, only single events have been selected as first approach for a feasibility study of the Compton camera application in ion range monitoring. All the results discussed in the following have been obtained with such an event selection.

The absolute camera efficiency variation as a function of the source position has been reported, with an ideal detector and with the application of detection energy thresholds in scatterer (50 keV) and absorber (100 keV). For low energies, below 2 MeV, the increased efficiency in the central section of the camera active surface - shown in Figure 8(a) - is linked to the increased relative number of photons approaching the camera with small angles. These photons are more likely undergoing Compton scattering with a reduced energy deposition, which is recorded by an ideal detector and rejected by the fixed energy threshold. The effect is all the more important as the primary gamma energy is limited, creating the peculiar energy dependence of the efficiency reduction observed in the results in Figure 8(b). Regarding the dependence of the efficiency on the Compton camera position, an accurate setup with respect to the expected Bragg peak position appears mandatory for the detection optimization.

The study of the signal-over-noise ratio as a function of beam intensity was performed (see Figure 9). The results show that, at clinical intensities, this ratio is very low. The TOF selection is effective in the case of carbon beams, where a significant proton and neutron contamination is expected. If we consider the case of proton beams, the amount of background and true coincidences is comparable at an intensity of about 1 proton per bunch, so that a clinical intensity reduction should be necessary to fit this configuration. The profile fall-off retrieval could not be achieved at clinical proton beam intensity for a single spot with the tested reconstruction methods. Even if a possible image reconstruction is not excluded by the low signal-over-noise ratio detected at realistic beam intensity with increased statistics (a group of spots with same expected range), given the fact that the background coincidences are distributed in an homogeneous way in the reconstructed volume, an intensity reduction can be an option in order to obtain more significant data sets. It must be noticed that the need for online check of Bragg peak position is all the more necessary for distal spots, which are in general the firsts to be treated, so that a beam intensity reduction at the beginning of the treatment can be foreseen in case an accurate monitoring is strictly needed. This would

not affect the treatment delivery, nor the planned patient rate in the clinical work-flow; indeed, the spreading of the time duration for few spots is of the order of one second. In the case of carbon ions, the larger amount of secondary neutron produced during the patient treatment seems to require other background rejection methods in order to lead to an advantageous signal-over-noise ratio. Note also that online filtering strategies may be used to improve the quality of the data (see Figure 7): already in Figure 9, one can notice that the amount of reconstructed events is about half that of true gamma, which means that partial absorption in the absorber leads to events which cannot be reconstructed via the line-cone method. More refined pre-analysis could be used and have been proposed in [Draeger et al., 2017]. Note also that the line-cone reconstruction used here is quite rough: the two reconstruction points are systematically considered, although further selection may refine the procedure and improve the profile quality (for instance, rejecting points outside the planned treatment volume). Alternative approaches for the optimization of the signal-over-noise ratio should be focused on the camera geometrical design. In [Fontana et al., 2017] we tested the same prototype with two absorber configurations, showing an absolute efficiency reduction of a factor approximately two when reducing the absorber from a 8×6 block matrix to a 3×3 one. Such a significant absorber size reduction is expected to drastically reduce the random coincidence contamination, thus improving the signal-over-noise ratio, with not dramatic efficiency degradation for the FOP monitoring purpose. Moreover, to this efficiency reduction corresponds an increased spatial resolution, probably given by the selection of gamma scattered with small angles. This hypothesis is confirmed by the efficiency variation generated by the applied energy thresholds, as discussed before. The design optimization could also foresee the reduction of the number of silicon layers, with a further expected reduction of the background coincidence rate. In addition to the aforementioned advantages, a more compact configuration allows for the implementation of several detector heads, which can be set at different angles and provide additional spatial information, in particular in view of 3D imaging. In case the highest possible efficiency is required, the distance between scatterer and absorber can also be modified, knowing that for reduced distances the efficiency is increased because a minimal amount of scattered photons escapes the absorber field of view. On the other hand, a reduction of the inter-detector distance is not recommended for accurate TOF measurements (for fixed target-scatterer distance), given the uncertainty added by the detectors time resolutions. In addition to this, also the spatial resolution is affected by a reduction of the scatterer-absorber distance, given the increased amount of photons scattered with large Compton angles included in the collected events. Indeed, large angle scatterings tend to degrade the spatial resolution. Dedicated design studies will be performed in the next future to address the proposed improvements.

The camera precision has been estimated for proton beams at the reduced intensity of 1 proton per bunch on average, starting from a reference prompt gamma emission profile obtained at high primary particle statistics (2×10^{10}), with the random extraction and reconstruction of 100 data subsets per number of incident protons and applying

a robust minimization algorithm to define the shift of the identified profile fall-off with respect to the reference one. The camera precision in the fall-off identification rapidly increases for increasing primary particle statistics. A sufficiently good precision is achieved on a spot basis for proton beams, where the precision is about 2.6 mm with a LM-MLEM reconstruction: a qualitative monitoring of each spot seems then possible. In order to achieve millimeter precision, some spot grouping methods must be considered, or multiple-head detector configurations, e.g in a ring geometry. As a general result, the LM-MLEM iterative algorithm, which is now the standard for this kind of image reconstruction, guarantees a better fall-off identification precision over the whole explored intensity range. However, LM-MLEM does not exploit the additional information provided by the knowledge of the beam position in the transverse plane. In future studies, such *a priori* information should be considered in order to improve the reconstruction rapidity and image quality. Moreover, the present version of the algorithm does not include regularization methods or image post-processing, and leads to the creation of reconstruction artifacts for increasing number of iterations. Improved version of the LM-MLEM algorithm are under study: regularization strategies could allow for exploiting a larger number of iterations thus increasing the contrast in the fall-off region and the consequent fall-off identification precision. In addition to this, more restrictive data selection during reconstruction can in principle improve the image quality and speed up the reconstruction process. At present, given the long calculation time required by the iterative algorithm, the line-cone reconstruction method can still be an option for on-line treatment check, when safety limit can be fixed in order to exclude severe deviation from the treatment planning and an interruption of the dose delivery in real time can be foreseen. Moreover, the TOF information can be included in the line-cone reconstruction method in order to constrain the emission on a single point, and improve its accuracy. Finally, it should be noticed that the presented study is focused on events involving one single scatterer layer: the inclusion of electron escape events can increase the reconstruction accuracy, given the constraint imposed on the reconstructed surface by the electron tracking information. Further study is needed to assess the gain in precision provided by such kind of events.

The Compton detection principle has already proven its potential in detecting prompt gammas for ion beam therapy monitoring purpose, and the CLaRyS Compton camera prototype shows promising results for this application. The detector is now at the final development stage, its components are being tested on beam in clinical facilities and a first beam test with a complete system is foreseen for the next year. New simulation studies are to be carried out to benchmark the Compton camera device to other detection systems, like PET machines or collimated detectors, already used or tested in clinics for ion beam therapy monitoring. The proposed study verify the feasibility of range monitoring in particle therapy with the CLaRyS Compton camera with a minimal approach, and improved performance are expected after detector and reconstruction method optimization.

Acknowledgments

References

[Aldawood et al., 2017] Aldawood, S., Thirolf, P. G., Miani, A., Böhmer, M., Dedes, G., Gernhäuser, R., Lang, C., Liprandi, S., Maier, L., Marinšek, T., Mayerhofer, M., Schaart, D. R., Valencia Lozano, I., and Parodi, K. (2017). Development of a Compton camera for prompt-gamma medical imaging. *Radiation Physics and Chemistry*, 140:190 – 197. 2nd International Conference on Dosimetry and its Applications (ICDA-2) University of Surrey, Guildford, United Kingdom, 3-8 July 2016.

[Andreyev et al., 2011] Andreyev, A., Sitek, A., and Celler, A. (2011). Fast image reconstruction for compton camera using stochastic origin ensemble approach. *Medical Physics*, 38(1):429–438.

[Bragg and Kleeman, 1904] Bragg, W. H. M. A. and Kleeman, R. (1904). On the ionization curves of radium. *The London, Edinburgh, and Dublin Philosophical Magazine and Journal of Science*, 8(48):726–738.

[Draeger et al., 2017] Draeger, E., Peterson, S., Mackin, D., Chen, H., Beddar, S., and Polf, J. C. (2017). Feasibility studies of a new event selection method to improve spatial resolution of Compton imaging for medical applications. *IEEE Trans Radiat Plasma Med Sci*, 1(4):358–367.

[Elsässer et al., 2004] Elsässer, T., Weyrather, W. K., Friedrich, T., Durante, M., Iancu, G., Krämer, M., Kragl, G., Brons, S., Winter, M., Weber, K.-J., and Scholz, M. (2004). Quantification of the relative biological effectiveness for ion beam radiotherapy: Direct experimental comparison of proton and carbon ion beams and a novel approach for treatment planning. *International Journal of Radiation Oncology Biology Physics*, 78(4):1177–1183.

[Enghardt et al., 2004] Enghardt, W., Crespo, P., Fiedler, F., Hinz, R., Parodi, K., Pawelke, J., and Pönisch, F. (2004). Charged hadron tumour therapy monitoring by means of PET. *Nuclear Instruments and Methods in Physics Research Section A: Accelerators, Spectrometers, Detectors and Associated Equipment*, 525(1):284 – 288. Proceedings of the International Conference on Imaging Techniques in Subatomic Physics, Astrophysics, Medicine, Biology and Industry.

[Fontana et al., 2017] Fontana, M., Dauvergne, D., Létang, J., Ley, J.-L., Testa, E., and Maxim, V. (2017). Versatile Compton camera for high-energy gamma rays: Monte carlo comparison with anger camera for medical imaging. *Acta Physica Polonica B*, 48:1639–1646.

[Fontana et al., 2018] Fontana, M., Dauvergne, D., Létang, J. M., Della Negra, R., Mounier, F., Zanetti, L., Zoccarato, Y., and Testa, E. (2018). Large surface gamma cameras for medical imaging: characterization of the bismuth germanate blocks. *Journal of Instrumentation*, 13(08):P08018.

[Frandes et al., 2010] Frandes, M., Zoglauer, A., Maxim, V., and Prost, R. (2010). A tracking Compton-scattering imaging system for hadron therapy monitoring. *IEEE Transactions on Nuclear Science*, 57(1):144–150.

[Gillam et al., 2011] Gillam, J. E., Lacasta, C., Torres-Espallardo, I., Candela Juan, C., Llosá, G., Solevi, P., Barrio, J., and Rafecas, M. (2011). A Compton imaging algorithm for on-line monitoring in hadron therapy. volume 7961, pages 79611O–79611O–8.

[Grevillot et al., 2011] Grevillot, L., Bertrand, D., Dessy, F., Freud, N., and Sarrut, D. (2011). A Monte Carlo pencil beam scanning model for proton treatment plan simulation using GATE/GEANT4. *Phys Med Biol*, 56(16):5203–5219.

[Hilaire et al., 2014] Hilaire, E., Robert, C., Lojacono, X., Sarrut, D., Buvat, I., Peyrin, F., and Maxim,

V. (2014). Compton imaging in proton therapy: reconstructed image of the simulated prompt-γ distribution. In *ICTR-PHE 2014*, page S43, Geneva, Switzerland.

[Hilaire et al., 2016] Hilaire, E., Sarrut, D., Peyrin, F., and Maxim, V. (2016). Proton therapy monitoring by Compton imaging: influence of the large energy spectrum of the prompt-gamma radiation. *Phys Med Biol*, 61(8):3127–3146.

[Huang et al., 2018] Huang, H.-M., Liu, C.-C., Jan, M.-L., and Lee, M.-W. (2018). A low-count reconstruction algorithm for compton-based prompt gamma imaging. *Physics in Medicine & Biology*, 63(8):085013.

[Knopf and Lomax, 2013] Knopf, A.-C. and Lomax, A. (2013). In vivo proton range verification: a review. *Phys Med Biol*, 58(15):R131–60.

[Kramer and Scholz, 2000] Kramer, M. and Scholz, M. (2000). Treatment planning for heavy-ion radiotherapy: calculation and optimization of biologically effective dose. *Phys Med Biol*, 45(11):3319–3330.

[Krimmer et al., 2017] Krimmer, J., Dauvergne, D., Létang, J., and Testa, E. (2017). Prompt-gamma monitoring in hadrontherapy: A review. *Nuclear Instruments and Methods in Physics Research Section A: Accelerators, Spectrometers, Detectors and Associated Equipment.*

[Krimmer et al., 2015] Krimmer, J., Ley, J.-L., Abellan, C., Cachemiche, J.-P., Caponetto, L., Chen, X., Dahoumane, M., Dauvergne, D., Freud, N., Joly, B., Lambert, D., Lestand, L., Magne, M., Mathez, H., Maxim, V., Montarou, G., Morel, C., Pinto, M., Ray, C., Reithinger, V., Testa, E., and Zoccarato, Y. (2015). Development of a Compton camera for medical applications based on silicon strip and scintillation detectors. *Nuclear Instruments and Methods in Physics Research Section A: Accelerators, Spectrometers, Detectors and Associated Equipment*, 787:98–101.

[Kuchment and Terzioglu, 2016] Kuchment, P. and Terzioglu, F. (2016). 3D Image Reconstruction from Compton camera data.

[Lojacono et al., 2013] Lojacono, X., Richard, M.-H., Ley, J.-L., Testa, E., Ray, C., Freud, N., Létang, J., Dauvergne, D., Maxim, V., and Prost, R. (2013). Low statistics reconstruction of the Compton camera point spread function in 3D prompt-γ imaging of ion beam therapy. *Nuclear Science, IEEE Transactions on*, 60(5):3355–3363.

[Mackin et al., 2012] Mackin, D., Peterson, S., Beddar, S., and Polf, J. (2012). Evaluation of a stochastic reconstruction algorithm for use in Compton camera imaging and beam range verification from secondary gamma emission during proton therapy. *Physics in Medicine and Biology*, 57(11):3537–3553.

[Maxim, 2018] Maxim, V. (2018). Enhancement of compton camera images reconstructed by inversion of a conical radon transform. *Inverse Problems*, 35(1):014001.

[McKisson et al., 1994] McKisson, J. E., Haskins, P. S., Phillips, G. W., King, S. E., August, R. A., Piercey, R. B., and Mania, R. C. (1994). Demonstration of three-dimensional imaging with a germanium Compton camera. *IEEE Transactions on Nuclear Science*, 41(4):1221–1224.

[Min et al., 2006] Min, C.-H., Kim, C. H., Youn, M.-Y., and Kim, J.-W. (2006). Prompt-gamma measurements for locating the dose falloff region in the proton therapy. *Applied Physics Letters*, 89(18):183517.

[Nadaraya, 1964] Nadaraya, E. A. (1964). On estimating regression. *Theory of Probability & Its Applications*, 9(1):141–142.

[Ordonez et al., 1997] Ordonez, C. E., Bolozdynya, A., and Chang, W. (1997). Doppler broadening and energy uncertainties in Compton cameras. *IEEE Nucl. Sci. Symp. Conf. Rec. 2 1361-65.*

[Ortega et al., 2015] Ortega, P. G., Torres-Espallardo, I., Cerutti, F., Ferrari, A., Gillam, J. E., Lacasta, C., Llosá, G., Oliver, J. F., Sala, P. R., Solevi, P., and Rafecas, M. (2015). Noise evaluation of Compton camera imaging for proton therapy. *Phys Med Biol*, 60(5):1845–1863.

[Paganetti, 2012] Paganetti, H. (2012). Range uncertainties in proton therapy and the role of Monte Carlo simulations. *Physics in Medicine and Biology*, 57(11):R99–R117.

[Parodi, 2016] Parodi, K. (2016). On- and off-line monitoring of ion beam treatment. *Nuclear Instruments and Methods in Physics Research Section A: Accelerators, Spectrometers, Detectors*

and Associated Equipment, 809:113 – 119. Advances in detectors and applications for medicine.

[Particle Therapy Cooperative Group, 2017] Particle Therapy Cooperative Group, P. (2017). Ptcog stats. *www.ptcog.ch.*

[Peters et al., 2008] Peters, A., Cee, R., Hoffmann, T., Reiter, A., Schwickert, M., and Winkelmann, T. (2008). Spill structure measurements at the Heidelberg Ion Therapy center. *Proceedings of EPAC08, Genoa, Italy.*

[Pinto et al., 2014] Pinto, M., Dauvergne, D., Freud, N., Krimmer, J., Letang, J. M., Ray, C., Roellinghoff, F., and Testa, E. (2014). Design optimisation of a tof-based collimated camera prototype for online hadrontherapy monitoring. *Phys Med Biol*, 59(24):7653–7674.

[Polf et al., 2015] Polf, J. C., Avery, S., Mackin, D. S., and Beddar, S. (2015). Imaging of prompt-gamma rays emitted during delivery of clinical proton beams with a Compton camera: feasibility studies for range verification. *Physics in Medicine and Biology*, 60(18):7085.

[Polf et al., 2009] Polf, J. C., Peterson, S., Ciangaru, G., Gillin, M., and Beddar, S. (2009). Prompt-gamma-ray emission from biological tissues during proton irradiation: a preliminary study. *Phys Med Biol*, 54(3):731–743.

[Robert et al., 2013] Robert, C., Dedes, G., Battistoni, G., Böhlen, T. T., Buvat, I., Cerutti, F., Chin, M. P. W., Ferrari, A., Gueth, P., Kurz, C., Lestand, L., Mairani, A., Montarou, G., Nicolini, R., Ortega, P. G., Parodi, K., Prezado, Y., Sala, P. R., Sarrut, D., and Testa, E. (2013). Distributions of secondary particles in proton and carbon-ion therapy: a comparison between GATE/Geant4 and FLUKA Monte Carlo codes. *Physics in Medicine and Biology*, 58(9):2879.

[Roellinghoff et al., 2014] Roellinghoff, F., Benilov, A., Dauvergne, D., Dedes, G., Freud, N., Janssens, G., Krimmer, J., Létang, J. M., Pinto, M., Prieels, D., Ray, C., Smeets, J., Stichelbaut, F., and Testa, E. (2014). Real-time proton beam range monitoring by means of prompt-gamma detection with a collimated camera. *Physics in Medicine and Biology*, 59(5):1327.

[Rogers, 2001] Rogers, D. F. (2001). *An Introduction to NURBS: With Historical Perspective.* Morgan Kaufmann Publishers Inc., San Francisco, CA, USA.

[Schoene et al., 2017] Schoene, S., Enghardt, W., Fiedler, F., Golnik, C., Pausch, G., Rohling, H., and Kormoll, T. (2017). An image reconstruction framework and camera prototype aimed for compton imaging for in-vivo dosimetry of therapeutic ion beams. *IEEE Transactions on Radiation and Plasma Medical Sciences*, 1(1):96–107.

[Schone et al., 2010] Schone, S., Shakirin, G., Kormoll, T., Herbach, C., Pausch, G., and Enghardt, W. (2010). A common approach to image reconstruction for different applications of Compton cameras. In *Nuclear Science Symposium Conference Record (NSS/MIC), 2010 IEEE*, pages 2292–2293.

[Smeets et al., 2012] Smeets, J., Roellinghoff, F., Prieels, D., Stichelbaut, F., Benilov, A., Busca, P., Fiorini, C., Peloso, R., Basilavecchia, M., Frizzi, T., C Dehaes, J., and Dubus, A. (2012). Prompt gamma imaging with a slit camera for real-time range control in proton therapy. 57:3371–405.

[Solevi et al., 2016] Solevi, P., Munoz, E., Solaz, C., Trovato, M., Dendooven, P., Gillam, J. E., Lacasta, C., Oliver, J. F., Rafecas, M., Torres-Espallardo, I., and Llosá, G. (2016). Performance of MACACO Compton telescope for ion-beam therapy monitoring: first test with proton beams. *Phys Med Biol*, 61(14):5149–5165.

[Stichelbaut and Jongen, 2003] Stichelbaut, F. and Jongen, Y. (2003). Verification of the proton beam position in the patient by the detection of prompt gamma-rays emission. *Proceeding of the 39th PTCOG meeting, San Francisco.*

[Taya et al., 2017] Taya, T., Kataoka, J., Kishimoto, A., Tagawa, L., Mochizuki, S., Toshito, T., Kimura, M., Nagao, Y., Kurita, K., Yamaguchi, M., and Kawachi, N. (2017). Optimization and verification of image reconstruction for a compton camera towards application as an on-line monitor for particle therapy. *Journal of Instrumentation*, 12(07):P07015.

[Testa et al., 2008] Testa, E., Bajard, M., Chevallier, M., Dauvergne, D., Le Foulher, F., Freud, N., Létang, J.-M., Poizat, J.-C., Ray, C., and Testa, M. (2008). Monitoring the bragg peak location of 73 MeV/u carbon ions by means of prompt γ-ray measurements. *Applied Physics Letters*,

93(9):093506.

[Testa et al., 2010] Testa, M., Bajard, M., Chevallier, M., Dauvergne, D., Freud, N., Henriquet, P., Karkar, S., Le Foulher, F., Letang, J. M., Plescak, R., Ray, C., Richard, M.-H., Schardt, D., and Testa, E. (2010). Real-time monitoring of the Bragg-peak position in ion therapy by means of single photon detection. *Radiat Environ Biophys*, 49(3):337–343.

[Todd et al., 1974] Todd, R. W., Nightingale, J. M., and Everett, D. B. (1974). A proposed γ camera. *Nature*, 251:132 EP –.

[Watson, 1964] Watson, G. S. (1964). Smooth regression analysis. *Sankhyā: The Indian Journal of Statistics, Series A (1961-2002)*, 26(4):359–372.

[Weyrather et al., 1999] Weyrather, W. K., Ritter, S., Scholz, M., and Kraft, G. (1999). RBE for carbon track-segment irradiation in cell lines of differing repair capacity. *Int J Radiat Biol*, 75(11):1357–1364.

[Wilderman et al., 1998] Wilderman, S. J., Clinthorne, N. H., Fessler, J. A., and Rogers, W. L. (1998). List-mode maximum likelihood reconstruction of compton scatter camera images in nuclear medicine. *1998 IEEE Nuclear Science Symposium Conference Record. 1998 IEEE Nuclear Science Symposium and Medical Imaging Conference (Cat. No.98CH36255)*, 3:1716–1720.

[Yamaya, 2018] Yamaya, T. (2018). Development of the openpet for in-beam carbon ion therapy imaging.

[Yoshihara et al., 2017] Yoshihara, Y., Shimazoe, K., Mizumachi, Y., Takahashi, H., Kamada, K., Takeda, A., Tsuru, T., and Arai, Y. (2017). Development of electron-tracking Compton imaging system with 30-μm SOI pixel sensor. *Journal of Instrumentation*, 12(01):C01045.

[Zoglauer et al., 2011] Zoglauer, A., Boggs, S. E., Galloway, M., Amman, M., Luke, P. N., and Marc Kippen, R. (2011). Design, implementation, and optimization of MEGAlib's image reconstruction tool Mimrec. *Nuclear Instruments and Methods in Physics Research Section A: Accelerators, Spectrometers, Detectors and Associated Equipment*, 652(1):568–571.